INTERNATIONAL JOURNAL OF AUTOMOTIVE AND MECHANICAL ENGINEERING
ISSN: 2229-8649 e-ISSN: 2180-1606
VOLUME 23, ISSUE 3, 2026, 13788 - 13800
DOI: https://doi.org/10.15282/ijame.23.3.2026.4.1040

RESEARCH ARTICLE

Development of a mathematical model and analysis of the impact of fuel system malfunctions on the dynamics of the diesel engine

Kamil Khafizov*, Artur Timirzyanov and Ramil Khafizov

Kazan State Agrarian University, 65 Karl Marx St., Kazan, 420015, Russia

Abstract – Conventional diagnosis of mechanically governed diesel fuel systems requires the removal and bench testing of pumps and injectors, whereas existing non-intrusive methods rarely relate crankshaft-speed features to specific physical faults. This study developed an integrated model of the MMZ D-243 four-cylinder diesel engine to quantify how wear and malfunctions in the fuel system distort crankshaft rotation. A single-zone first-law cylinder model with Wiebe heat release was coupled to slider-crank dynamics and parametric sub-models of the in-line UTNM pump, hydromechanical injectors, and air path. Seven fault families were simulated in MATLAB from idle to rated speed and from 30% to full load. Faults that unbalance cyclic fuel delivery dominate the coefficient of rotational unevenness: single-section plunger wear increases it by 19.6%, pump-section maladjustment by 13.6%, and delivery valve leakage by 9.3%. Uniform air or fuel starvation slightly reduced the coefficient but decreased the power by up to 32%. Wall heat transfer, operating point, sensitivity, and Monte Carlo analyses preserve the fault ranking. A cylinder-resolved peak-acceleration ratio separates the faulty and healthy cases by approximately eight standard deviations, whereas the global coefficient provides only approximately two. Therefore, a diagnostic threshold of 0.94 was proposed for cylinder-by-cylinder screening.

Article History
Received : 17 April 2026
Revised : 22 June 2026
Accepted : 16 July 2026
Published : 25 September 2026

Keywords
Diesel engine
Diagnostics
Mathematical modelling
Fuel system
Rotational unevenness
High-pressure fuel pump (HPFP)

1. Introduction

Mechanically governed diesel engines remain widely used in agricultural and off-road machinery, where reliable field diagnosis is important because the removal of the high-pressure fuel pump and injectors for bench testing is time-consuming and can introduce additional assembly errors. Injection system settings strongly influence diesel engine performance and emissions [1], whereas the wear of precision injector components degrades both the operating and environmental characteristics [2]. The analysis of dynamic fuel-rail pressure can identify pump and injector faults [3], but it relies on access to the fuel-pressure signal. Therefore, a low-cost method based on signals already available on the engine is desirable. The instantaneous crankshaft rotational speed and the angular acceleration derived from it are attractive because both respond directly to the torque contribution of each cylinder. Early studies have demonstrated diesel-fault detection based on instantaneous angular speed [4]. Subsequent condition-monitoring studies established a practical speed-based diagnosis [5] and showed that malfunctions can be localised from the rotational signal of multi-cylinder engines [6]. Recent studies have extended this approach using data-driven methods, including digital twin attention networks [7], time–frequency and vision transformer models [8], long short-term memory (LSTM) classifiers using crank speed [9], and domain-adaptive convolutional networks designed specifically for noisy cross-domain misfire diagnosis [10]. Crank-angular-velocity-based misfire detection has been refined by correcting for in-cylinder gas properties [11]. Instantaneous-speed methods have been applied to dual-fuel engine misfire diagnosis [12], direct localisation of the faulty cylinder in multi-cylinder diesel engines [13], and multi-speed misfire classification [14].

Complementary work uses vibration, in-cylinder pressure, spectral features and multi-sensor monitoring. Machine-learning misfire identification has been demonstrated for marine engines [15], and pressure-based data models have been developed for engine-fault diagnosis [16]. Recent studies based on spectral analysis [17], vibration condition monitoring [18], airflow sensor failure detection [19], and real-time convolutional networks [20] illustrate the breadth of available signals. Earlier studies on diesel engine vibrations and acoustic emissions support non-intrusive monitoring [21]. Related IJAME work demonstrates neural network residual-based fault detection in rotating machinery using existing process variables [22] and shows that diesel engine acoustic features vary systematically with operating conditions [23]. Data-driven performance and combustion models have also advanced: regression and neural network approaches predict diesel performance [24], supervised learning evaluates dual biodiesel blends [25], numerical models assess post-injection in diesel-syngas combustion [26], and cycle-resolved studies quantify combustion variability [27]. Nevertheless, two gaps remain. First, the most recent methods either require large labelled datasets or are specific to one experimental engine, and they do not directly map a measured crankshaft speed feature to a named physical parameter of a mechanically governed pump-line-nozzle system. Second, diagnostic recommendations are commonly qualitative, and a statistically grounded threshold that separates a weak cylinder from cycle-to-cycle scatter has rarely been reported.

Therefore, the aim of this study was to develop an integrated mathematical model of the MMZ D-243 diesel engine, quantify and rank the effects of the main fuel system faults on crankshaft rotational unevenness, and derive a cylinder-resolved diagnostic feature with a quantitative detection threshold. The study couples cylinder thermodynamics, crank-mechanism dynamics, and parametric fuel equipment sub-models; verifies numerical convergence; evaluates fault scenarios across speed and load; quantifies parameter sensitivity and uncertainty; and compares the proposed feature with

*CORRESPONDING AUTHOR | K. Khafizov| ✉ fts-kgau@mail.ru
© 2026 The Author(s). Published by Universiti Malaysia Pahang Al-Sultan Abdullah Press. This is an open access article under the CC BY-NC 4.0 license

alternative diagnostic routes. The contribution is not a new combustion law but a physically interpretable link between specific fuel-equipment defects and the instantaneous speed signature, along with a statistically supported criterion for cylinder-by-cylinder screening.

2. Materials and Methods

2.1 Object of Study

The object of study is the MMZ D-243, a four-cylinder, four-stroke, naturally aspirated direct injection diesel engine; a turbocharged variant is also considered where noted. Its principal specifications are listed in Table 1. The engine is fitted with an in-line UTNM pump delivering injection pressures up to approximately 20 MPa, closed hydromechanical injectors, and a three-stage dry air cleaner. Figure 1 shows the test engine used as the reference for the model parameters, and Figure 2 defines the forces and geometry of the crank mechanism.

Table 1. Specifications of the MMZ D-243 diesel engine

Parameter	Symbol	Value	Unit
Engine type	–	In-line 4-cyl., 4-stroke, DI diesel	–
Number of cylinders	i	4	–
Total displacement	V_h	4.75	L
Cylinder bore	D	110	mm
Piston stroke	S	125	mm
Connecting-rod length	L	240	mm
Crank radius	R	62.5	mm
Compression ratio	ε	16	–
Firing order	–	1–3–4–2	–
Rated power	N_e	59.6 (81)	kW (hp)
Rated speed	n	2200	rpm
Maximum torque	M_max	298	N·m
Injection pump	–	In-line UTNM, plunger type	–
Maximum injection pressure	p_inj	≈ 20	MPa
Injector	–	Closed, hydromechanical	–
Air cleaner	–	Three-stage, dry	–

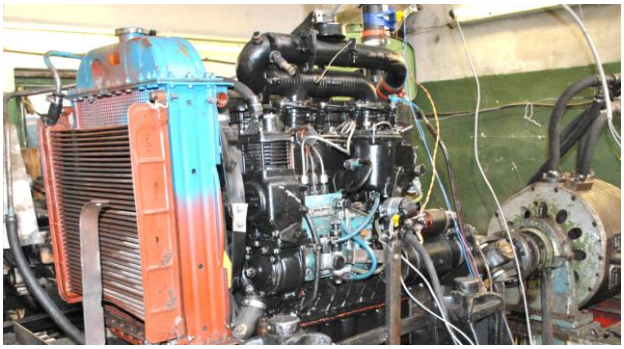


Figure 1. View of the D-243 engine on the test stand

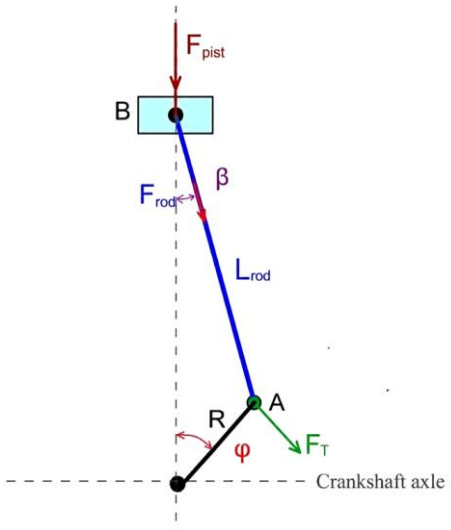


Figure 2. Forces and geometry of the crank mechanism

2.2 Mathematical Model

The model is a coupled system of differential and algebraic equations describing, for each cylinder, the air charging, fuel delivery, combustion, and the resulting gas torque, together with the rotational dynamics of the crankshaft assembly. The cylinders are treated as identical in geometry but are supplied and phased individually, allowing a fault localised to one section or one injector to be represented and tracked through to the crankshaft signal.

2.2.1 Crankshaft dynamics

The backbone of the model is the rotational form of Newton's second law for the crankshaft assembly [28],

$$J_{red}\frac{d\omega}{dt}=\sum_{i=1}^{4}M_i(\varphi_i)-M_r(\omega),\qquad \frac{d\varphi}{dt}=\omega,\qquad \frac{d\omega}{dt}=\alpha \tag{1}$$

where J_{red} is the reduced moment of inertia of the rotating and reciprocating masses referred to the crankshaft (kg·m²), ω is the angular velocity (rad/s), φ is the crank angle (rad), M_i is the instantaneous torque produced by the i-th cylinder (N·m), and M_r is the resistance torque from the external load and mechanical losses (N·m). The total engine torque is obtained by superposition of the individual cylinder contributions, each shifted by the phase of its working cycle,

$$M_{eng}(\varphi)=\sum_{i=1}^{N_{cyl}}M_i(\varphi-\Delta\varphi_i) \tag{2}$$

where Ncyl is the number of cylinders and Δφi is the phase offset of cylinder i relative to the first. For the D-243 firing order 1–3–4–2, the power strokes follow every 180°, so the offsets are 0°, 180°, 360°, and 540° for cylinders 1, 3, 4, and 2, respectively, and the full cycle spans 720°. The torque of one cylinder is derived from the gas force on the piston and the exact slider-crank geometry shown in Figure 2 [29],

$$M_i(\varphi)=p_i(\varphi)\frac{\pi D^2}{4}\frac{S}{2}\left[sin\varphi+\frac{\lambda}{2}\frac{sin2\varphi}{\sqrt{1-\lambda^2 sin\varphi^2}}\right] \tag{3}$$

where p_i is the in-cylinder pressure (Pa), the piston area is $A_p=\pi D^2/4$, and $\lambda=R/L\approx 0.26$ is the crank-to-rod ratio. The bracketed kinematic factor includes the connecting rod obliquity, so the model retains the asymmetry of the tangential force between the first and second halves of the stroke rather than assuming an infinitely long rod. Because the crankshaft speed is not constant within a cycle, the coefficient of rotational unevenness is defined as

$$\delta=\frac{\omega_{\max}-\omega_{\min}}{\omega_m} \tag{4}$$

where ω_{max}, ω_{min}, and ω_m are the maximum, minimum, and mean angular velocities over one cycle. A rise in δ reflects a larger relative swing in speed and is the integral indicator of cylinder imbalance used throughout this study.

2.2.2 In-cylinder thermodynamics

The working process of each cylinder is represented as a single open zone and described by the first law of thermodynamics. Using the ideal gas relation and the standard energy balance gives [30], [31]

$$\frac{dp}{d\varphi}=\frac{1}{V(\varphi)}\left[(\gamma-1)\frac{dQ}{d\varphi}-\gamma p\frac{dV}{d\varphi}\right] \tag{5}$$

where V is the instantaneous cylinder volume (m³), γ is the ratio of specific heats, and $dQ/d\varphi$ is the net heat-release rate (J/rad). The derivation follows the standard route: for an ideal gas the internal energy is $U=m_{cv}T$, Mayer's relation and the equation of state are used to express temperature through p and V, and after substituting the heat input and the displacement work $dW=p\,dV$ the result is rearranged into the form above. Two different values of γ are used for the compression and expansion parts of the cycle to reflect the change in charge composition and temperature. The cylinder volume is computed from the exact slider-crank kinematics,

$$V(\varphi)=V_c+\frac{\pi D^2}{4}\cdot\frac{S}{2}\left[(1-\cos\varphi)+\frac{1}{\lambda}\left(1-\sqrt{1-\lambda^2\sin\varphi^2}\right)\right] \tag{6}$$

with Vc the clearance volume fixed by the compression ratio. Heat release is represented by the Wiebe function [32]; the burned-mass fraction and its rate are

$$x(\varphi)=1-\exp\left[-a\left(\frac{\varphi-\varphi_0}{\Delta\varphi_z}\right)^{m+1}\right] \tag{7}$$

$$\frac{dQ}{d\varphi}=\frac{Q_c a(m+1)}{\Delta\varphi_z}\left(\frac{\varphi-\varphi_0}{\Delta\varphi_z}\right)^m exp\left[-a\left(\frac{\varphi-\varphi_0}{\Delta\varphi_z}\right)^{(m+1)}\right] \tag{8}$$

where φ_0 is the start of combustion, $\Delta\varphi_z$ the combustion duration, m the shape factor, and $a=6.908$ sets 99.9% completion at the end of the burn. The shape factor m controls the curvature of the release (Figure 3). Poor preparation of the mixture,

for example through nozzle coking or low injection pressure, makes combustion more sluggish, which appears in the model as a larger $\Delta\varphi_z$ and a lower m. The total heat available per cycle is tied to the delivered fuel,

$$Q_c = g_c H_u \eta_{comb} \tag{9}$$

with g_c the cyclic fuel mass, H_u = 42.5 MJ/kg the lower heating value, and η_{comb} a combustion-efficiency factor.

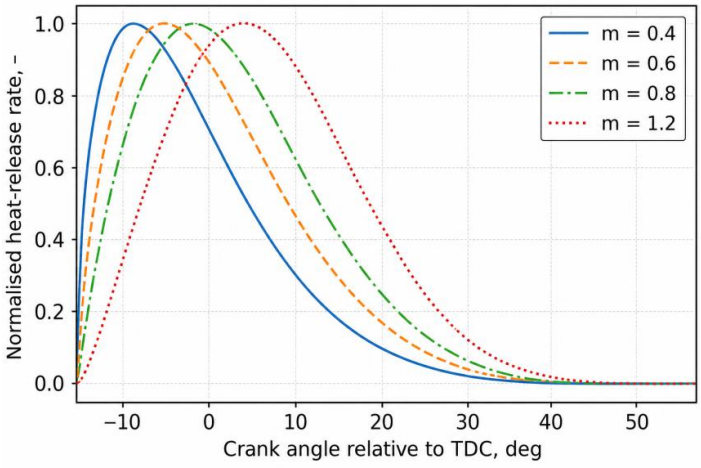


Figure 3. Heat-release rate for several values of the Wiebe shape factor m

Baseline calculations initially neglect heat exchange with the cylinder walls so that the influence of the fuel system can be isolated. To evaluate the impact of this simplification, a convective wall-loss term based on the Woschni correlation [33] was implemented as a separate option and used to test the robustness of the conclusions (Section 3.6):

$$\frac{dQ_w}{d\varphi} = \frac{h_c A_w (T - T_w)}{\omega}, \quad h_c = 3.26 D^{-0.2} p^{0.8} T^{-0.55} \left(C_1 c_m\right)^{0.8} \tag{10}$$

Here h_c is the convective coefficient (W/m²·K), A_w the instantaneous heat-transfer area, T and T_w the gas and wall temperatures, c_m the mean piston speed, and C_1 a gas-velocity constant. The term is subtracted from the heat-release rate in Eq. (5) when the wall-loss option is active.

2.2.3 Air supply system

The three-stage dry air cleaner is represented by its effect on the volumetric efficiency. In the naturally aspirated configuration, the intake pressure is close to ambient, and growing restriction across the filter lowers the pressure available to fill the cylinder. The reduced volumetric efficiency η_v decreases the trapped air mass, which in turn worsens combustion and is represented in the model as a higher $\Delta\varphi_z$ and a lower shape factor. In the turbocharged configuration the boost pressure raises η_v above unity and allows more fuel to be burned for a given displacement; the sensitivity to filter condition is retained because intake restriction also lowers the pressure ratio across the compressor.

2.2.4 Fuel supply system

The fuel system sets the parameters that drive the combustion sub-model. For the in-line UTNM pump the cyclic delivery is the geometric stroke volume reduced by the leakage that escapes through the plunger-barrel clearance under injection pressure,

$$g_c = g_{geom} - g_{leak} \tag{11}$$

where g_{geom} is the geometric delivery fixed by the active plunger stroke and rack position, and g_{leak} is the back leakage per cycle. The leakage is estimated from the laminar film flow through the annular clearance; thus, it increases with the cube of the radial gap, pressure difference across the plunger, and injection duration, and decreases with the fuel viscosity and overlap length. A pressure-wave-resolved treatment of a diesel fuel system was described in [34]; the present cycle-integrated model deliberately retains only the quantities that determine the released energy. Plunger-pair wear widens the clearance and sharply lowers the effective delivery, which is the physical origin of fault scenario S1. Fuel issuing from the injector is computed from the orifice-flow equation [35],

$$\dot{m} = \mu_{inj} A_{eff} \sqrt{2\rho\left(p_f - p_{cyl}\right)} \tag{12}$$

where μ_{inj} is the discharge coefficient, A_{eff} is the effective nozzle area, ρ is the fuel density, and $p_f - p_{cyl}$ is the pressure drop across the holes. Coking reduces the effective area, whereas wear may enlarge it and reduce the effective injection pressure. Both defects are represented by A_{eff}, injector opening pressure, and combustion duration and shape parameters.

Three hydraulic effects are deliberately left out of this sub-model: the compressibility of the fuel in the high-pressure line, the dynamics of the needle as a moving body, and the propagation of pressure waves along the pipe. These phenomena shape the fine structure of the injection rate trace and the cycle-to-cycle pressure pulsations, and their detailed

treatment is a field in its own right. For the present purpose, however, the quantity that couples to the rotational signal is the heat released per cycle, which is fixed by the cycle-integrated delivered mass through Eqs. (9) and (11); the higher frequency hydraulic detail redistributes the injection within a cycle but changes the per-cycle energy balance only slightly. A coupled hydraulic model of the line and nozzle is identified as future work in Section 4.

2.3 Fault Scenarios and Choice of Severities

Each fault was introduced by changing the model parameters that it physically affected, as summarised in Table 2. Seven families are considered: S1, wear of the plunger pair of one section, modelled as a 30% loss of that section's cyclic delivery; S2, coking of an injector nozzle; S3, maladjustment of the pump sections, modelled as a ±15% spread in delivery between cylinders; S4, leakage of a delivery valve; S5, a drop in injector opening pressure; S6, air-filter restriction at 10%, 40%, and 60%; and S7, fuel-filter clogging or low-pressure-pump wear, again at 10%, 40%, and 60%. The severity levels are not arbitrary; they bracket the range of services. The 30% delivery loss assigned to single-section plunger wear corresponds to the clearance growth at which the pump-overhaul practice condemns a plunger pair, while the ±15% spread used for maladjustment is the band beyond which sections are re-trimmed on the bench. For the filters, the 10% level represented a lightly fouled element that was still within its service interval, 40% approximated the intake-restriction rise at which replacement was recommended, and 60% represented a neglected, severely clogged element. The intent is to span light, marginal, and severe conditions rather than to fix a single representative value so that the trends rather than one specific number carry the diagnostic message.

Table 2. Representation of the main fuel system faults through model parameters

Fault / wear	Change in model parameters	Expected effect on acceleration α and power N
Plunger-pair wear (one section)	g_{leak} ↑ (Eq. 11), g_c ↓, Q_c ↓	Sharp drop in α peak of that cylinder; clear loss of its power contribution
Delivery-valve leakage	Lower residual pressure; later φ_0; g_c ↓	α peak shifted later and reduced; moderate power loss
Reduced injector pressure (p_{inj})	Earlier φ_0; poorer atomisation ($\Delta\varphi_z$ ↑, m ↓)	Altered shape of the α curve; small power loss
Nozzle coking	A_{eff} ↓ (Eq. 12); $\Delta\varphi_z$ ↑, m ↓	Sluggish acceleration, lower α peak; power loss
Nozzle-hole wear	A_{eff} ↑; lower pressure, poorer atomisation	Lower α peak; power loss
Pump-section maladjustment	Cylinder-to-cylinder spread in g_c	Marked scatter of α peaks between cylinders
Air-filter restriction	Δp_{filter} ↑, η_v ↓ in all cylinders	Uniform fall in α; overall power loss
Fuel-filter / LPFP wear	Lower pressure upstream of the HPFP; g_c ↓ under load	Uniform fall in α under load; overall power loss

2.4 Numerical Implementation and Verification

The equations were integrated in MATLAB using an adaptive explicit Runge–Kutta scheme (Dormand–Prince pair). Each cylinder was advanced over its closed period with relative and absolute tolerances of 10^{-6}, and the cylinder torques were superimposed on a common crank angle grid of 0.5° to form the engine torque, from which the speed and acceleration were obtained. The baseline parameters were calibrated so that the indicated power and torque reproduced the rated figures of the D-243: the computed 61.0 kW and 291 N·m at 2000 rpm corresponded to the rated 59.6 kW and 298 N·m when a mechanical efficiency of approximately 0.93 was applied. This anchors the absolute model baseline to the specified engine performance level. The independence of the result from the discretisation was checked by halving the integration step and tightening the tolerances. As shown in Table 3, the baseline coefficient of rotational unevenness changes by less than 2% as the step is reduced from 2° to 0.1°, and the fault increment for S1 settles to within a few tenths of a percentage point. The working grid of 0.5° with a tolerance of 10^{-6} lies within this converged region and was used for all the subsequent calculations.

Table 3. Independence of the baseline solution from integration step and tolerance

Step (deg)	Tolerance (rel.)	δ baseline	Δδ for S1 (%)
2.0	10^{-4}	0.011850	18.30
1.0	10^{-5}	0.011796	19.21
0.5	10^{-6}	0.011770	19.64
0.25	10^{-7}	0.011754	19.88
0.1	10^{-8}	0.011744	20.02

3. Results and Discussion

3.1 Baseline and Parametric Results

Table 4 lists the power, torque, rotational unevenness coefficient, and relative change for the baseline engine and each fault scenario at 2000 rpm. The calculated power is the indicated value, and the comparison of interest is the relative

response of δ to each defect in the sensor. The healthy engine had $\delta \approx 0.0118$. The largest increase, to 0.0141, was caused by plunger pair wear in a single section, followed by maladjustment of the sections and delivery valve leakage. In contrast, the air- and fuel-restriction scenarios reduce the average torque and power but do not amplify the imbalance; therefore, they leave δ slightly lower, whereas power decreases steeply, by as much as 32% in the most severe fuel starvation case.

Table 4. Parametric modelling of MMZ D-243 faults at 2000 rpm

Scenario	Power [kW]	Torque [N·m]	δ [–]	Δδ [%]
Baseline	60.97	291.1	0.0118	+0.0
S1: plunger wear (cyl. 3)	56.77	271.1	0.0141	+19.6
S2: injector coking (cyl. 3)	60.75	290.0	0.0118	+0.6
S3: pump maladjustment	60.97	291.1	0.0134	+13.6
S4: delivery valve (cyl. 3)	58.87	281.1	0.0129	+9.3
S5: injector pressure (cyl. 3)	60.79	290.3	0.0118	+0.4
S6: air filter (10%)	60.81	290.4	0.0117	−0.4
S6: air filter (40%)	60.44	288.6	0.0117	−0.7
S6: air filter (60%)	60.07	286.8	0.0117	−1.0
S7: fuel filter / LPFP (10%)	58.18	277.8	0.0115	−2.2
S7: fuel filter / LPFP (40%)	49.77	237.7	0.0108	−8.5
S7: fuel filter / LPFP (60%)	41.38	197.6	0.0100	−14.8

3.2 Indicator Diagrams

Figure 4 compares the pressure traces of cylinder 3 for the baseline and two representative fault cases. A defect that reduces the actual delivery, as in S1, lowers the peak pressure because less fuel was burned. Coking, S2, acts differently: the pressure maximum moves to a later angle and the rise becomes flatter, which is the signature of delayed and sluggish combustion rather than a smaller heat input.

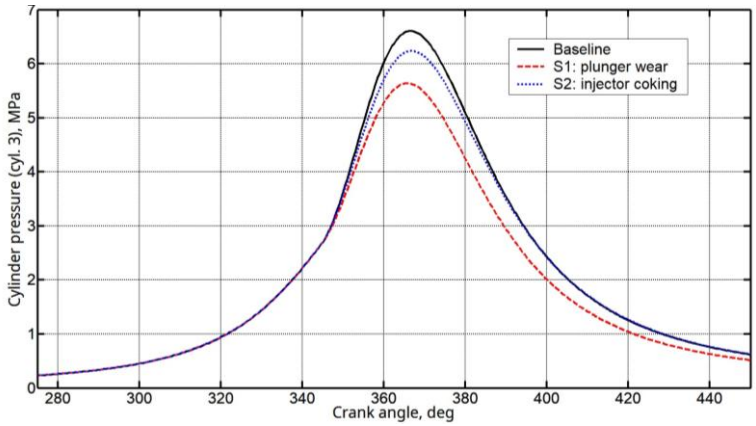


Figure 4. In-cylinder pressure for the baseline and two fault scenarios

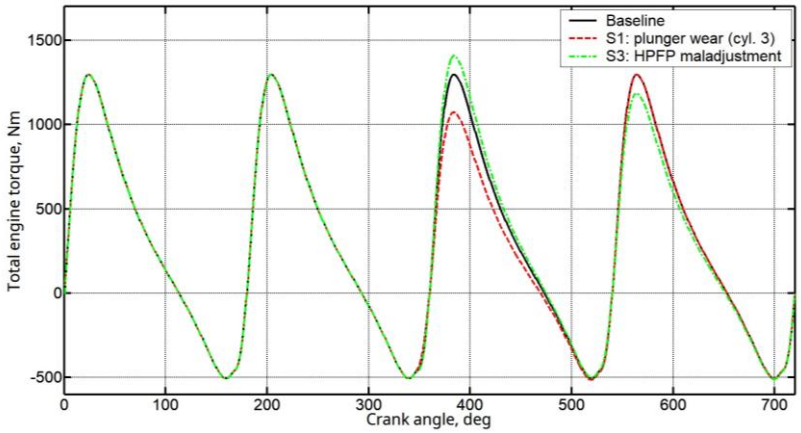


Figure 5. Engine torque for the baseline and two fault scenarios

3.3 Torque

The engine torque responds not only to the mean heat-release level but also to the distribution of work among the cylinders. Figure 5 shows a local dip in the power stroke segment of the affected cylinders S1 and S3. Because the dip is locked to the phase of one cylinder, it can be attributed to that cylinder, thereby enabling a cylinder-by-cylinder diagnosis.

3.4 Angular Acceleration

The angular acceleration follows from the equation of motion as the time derivative of the crankshaft speed,

$$\alpha(\varphi) = \frac{d\omega}{dt} \tag{13}$$

The quantity is computed for each cylinder over its power stroke. Angular acceleration is the most informative signal examined. In Figure 6, fault S1 produces a clear reduction in the positive acceleration peak during the power stroke of the third cylinder, while the other peaks remain nearly unchanged. Under S3, mean engine power changes little, yet the acceleration peaks diverge between cylinders, as expected for section maladjustment that redistributes an almost unchanged mean energy input. This selective, phase-locked behaviour is the basis of the diagnostic feature developed in Section 3.9.

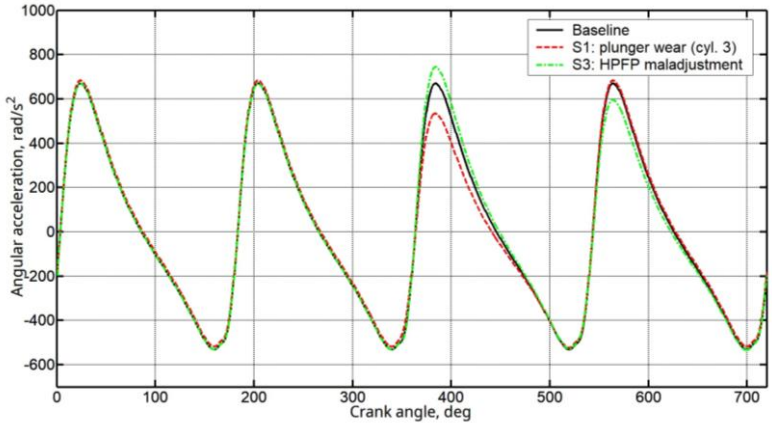


Figure 6. Crankshaft angular acceleration for the baseline and two fault scenarios

3.5 Angular Velocity and Filter Clogging

The instantaneous angular velocity in Figure 7 shows the same effect from a different perspective: a fault that weakens one cylinder deepens the deceleration following the power stroke of that cylinder. Therefore, the rotational unevenness coefficient is more sensitive to local fuel system faults than to uniform loss of power. Figure 8 shows the contrasting responses to the fuel filter and low-pressure-line restriction. As the restriction increased, the torque amplitude decreased approximately uniformly across the cycle; the weakening was global rather than cylinder-specific; thus, it appeared mainly as a power loss rather than an increase in rotational unevenness.

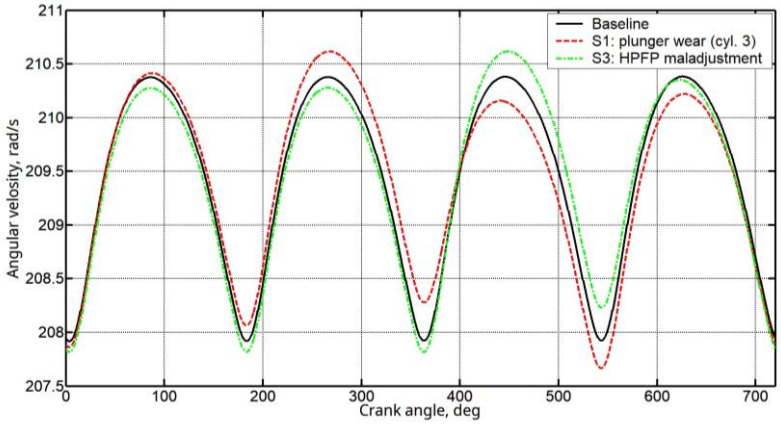


Figure 7. Fluctuation of crankshaft angular velocity

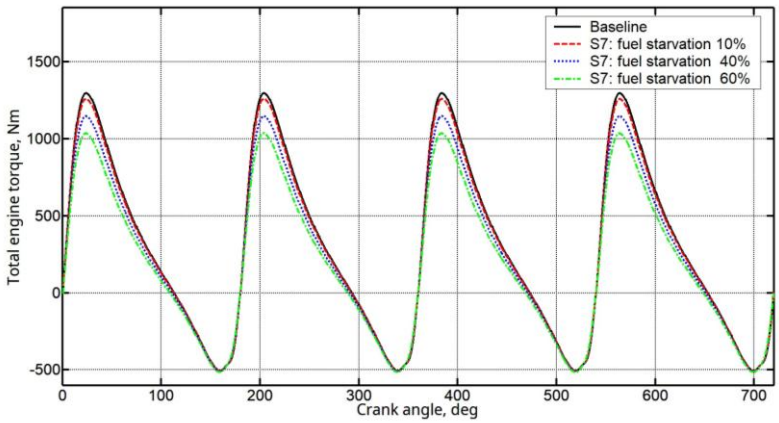


Figure 8. Effect of fuel-filter restriction on engine torque

3.6 Effect of Wall Heat Transfer

To test whether neglecting wall heat transfer in the baseline distorts the conclusions, the Woschni term in Eq. (10) was activated, and the calculations were repeated. The effect on the absolute level is appreciable: the baseline indicated power falls from 61.0 to 54.5 kW, approximately 11%, which brings the model closer to the rated brake figure, and the peak cylinder pressure is slightly reduced (Figure 9, left). However, the effect on the diagnostic ranking was small. As shown in the right panel of Figure 9, the fault increments shift only modestly when heat transfer is included: S1 from +19.6 to +17.9%, S3 from +13.6 to +12.4%, S4 from +9.3 to +7.7%, and the severe fuel-starvation case S7 from −8.5 to −7.9%. The order of the faults and the sign of every response are unchanged; therefore, the omission of wall losses in the baseline affects the absolute numbers but not the physical interpretation or the ranking on which the diagnostic rests.

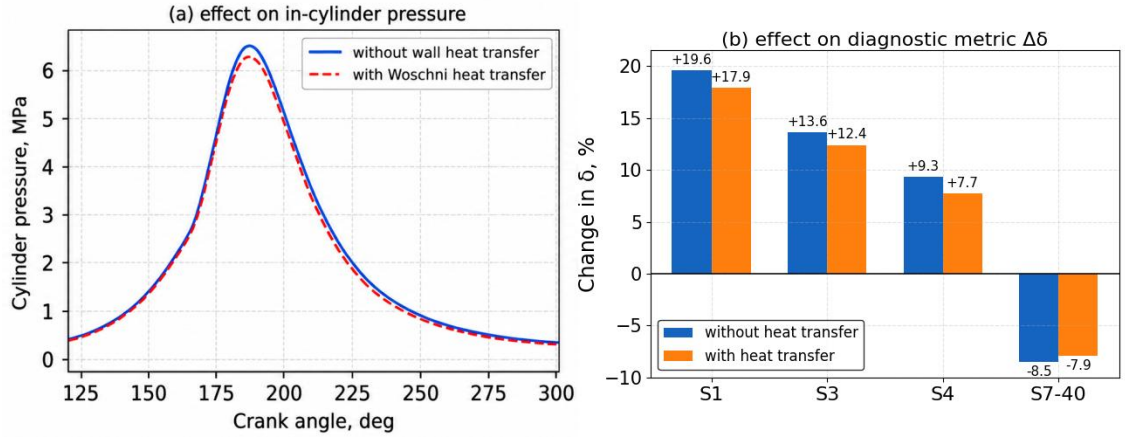


Figure 9. Robustness to wall heat transfer: effect on cylinder pressure (left) and on the diagnostic metric Δδ (right)

3.7 Behaviour Across Speeds and Loads

The fault signature must survive the change in the operating point if it is to be useful in the field. Therefore, the model was run over a grid spanning idle to rated speeds and from part-to full-load conditions. The results for the baseline and plunger wear fault S1 are presented in Table 5 and Figure 10. The healthy coefficient itself increases at low speed and load, from approximately 0.012 at the rated point to 0.052 near idle, which is expected because fewer and weaker power strokes act on the same inertia. The S1 increment persists clearly throughout: it is +8.4% at 800 rpm and 30% load, +15.0% at 1400 rpm and 65% load, close to +19.6% at full load between 2000 and 2200 rpm, and +12.5% at 2000 rpm and at half load. The fault is thus detectable across the entire working envelope, although the baseline against which it is measured must be considered at a comparable operating point.

Table 5. Baseline and S1 fault across operating points

Speed [rpm]	Load [%]	Power [kW]	δ baseline [–]	Δδ for S1 [%]	Δδ for S3 [%]
800	30	8.7	0.0519	+8.4	+5.9
1400	65	29.0	0.0205	+15.0	+10.4
2000	100	61.0	0.0118	+19.6	+13.6
2200	100	67.1	0.0097	+19.6	+13.6
2000	50	33.0	0.0093	+12.5	+8.7

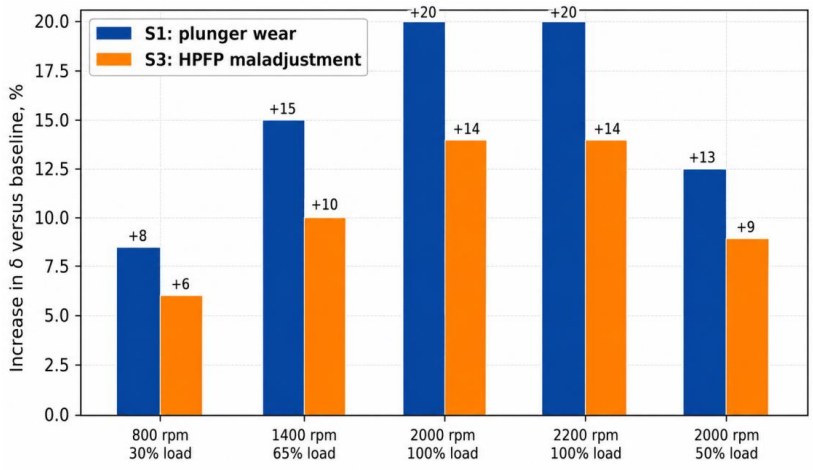


Figure 10. Increase in rotational unevenness for fault S1 across speed and load

3.8 Parameter Sensitivity

A one-at-a-time sensitivity study quantified how strongly δ responded to each model input. Every parameter was perturbed by ±10% about the baseline, and the mean absolute change in δ recorded; the sensitivity coefficient of Eq. (16) normalised this response. The ranking in Table 6 and Figure 11 is clear and unambiguous. The reduced inertia dominates, with a 10.1% mean change; however, it is a calibration constant rather than a fault and simply scales the whole signal as $\delta \propto 1/J$. The next parameter is the cyclic delivery of a single cylinder, at 6.93%, and the imbalanced nature of its effect is revealed by the fact that both positive and negative perturbations raise δ. A uniform change in the mean fuelling across all cylinders moves δ by approximately half as much, 4.2%, whereas injection timing, combustion duration, and the Wiebe shape factor are an order of magnitude weaker at 0.46%, 0.32%, and 0.03%, respectively. The picture is internally consistent: rotational unevenness is controlled by the balance of delivery between cylinders far more than by the quality of atomisation, which explains why supply imbalance faults head the ranking in Table 4, while coking and low injection pressure barely register. In practice, this also means that the inertia must be known accurately for the absolute δ to be trusted, whereas the cylinder-to-cylinder comparison used for diagnosis is unaffected by it.

Table 6. Sensitivity of the rotational-unevenness coefficient to model parameters (±10% perturbation)

Parameter	Δδ at +10% [%]	Δδ at −10% [%]	Mean |Δδ| [%]
Reduced inertia J_red	−9.09	+11.11	10.10
Single-cylinder fuelling g_c	+7.67	+6.18	6.93
Mean fuelling (all cylinders)	+4.23	-4.25	4.24
Injection timing φ_0	+0.06	+0.86	0.46
Combustion duration Δφ_z	+0.09	+0.55	0.32
Wiebe shape factor m	-0.01	+0.05	0.03

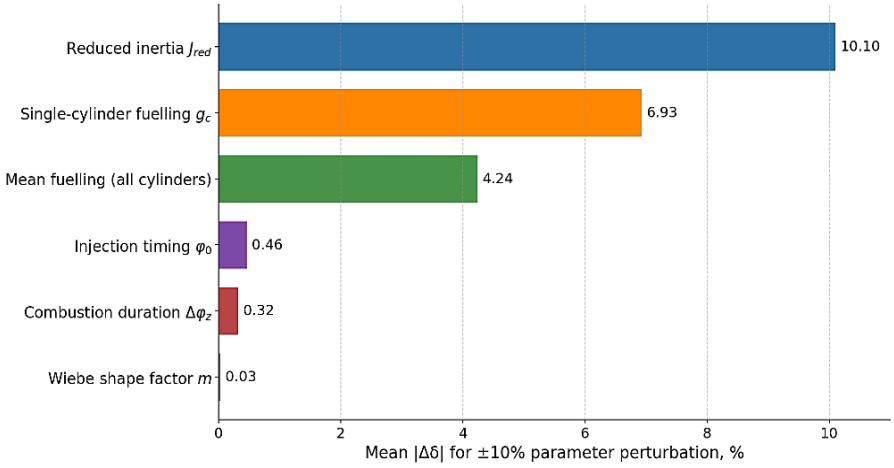


Figure 11. Sensitivity of the rotational-unevenness coefficient to a ±10% change in each model parameter

3.9 Uncertainty and Diagnostic Thresholds

A diagnostic feature is useful only if it separates a fault from the natural signal scatter. Therefore, cycle-to-cycle variability was imposed as random perturbations of ±3% in per-cylinder fuelling and ±5% in the remaining parameters, and 400

cycles were generated for the healthy engine and fault S1. Figure 12 shows that the global coefficients δ for the healthy (0.0122 ± 0.0006) and faulty (0.0142 ± 0.0007) engines overlap within approximately two standard deviations. Therefore, a single global scalar metric is unreliable when realistic scatter is included. The cylinder-resolved feature behaves differently for different values of. Defining the per-cylinder peak-acceleration ratio.

$$R_k = \frac{\alpha_k^{peak}}{\max_j \alpha_j^{peak}}, \qquad k = 1,\ldots,4 \tag{14}$$

as the smallest cylinder's acceleration peak divided by the largest, the healthy engine clusters at 0.976 ± 0.011 while the faulty engine falls to 0.827 ± 0.015, a separation of about eight standard deviations. A cylinder is therefore flagged when

$$\min_k R_k < R_{thr}, \qquad R_{thr} = \mu_R - 3\sigma_R \tag{15}$$

with the threshold Rthr = μR − 3σR ≈ 0.94 set three standard deviations below the healthy mean. Fault S1 violates this limit by nearly eight standard deviations and is therefore detected with high probability; under a Gaussian assumption, a one-sided three-standard-deviation threshold corresponds to a false alarm probability of approximately 0.13%. The sensitivity coefficient used in Section 3.8 is defined consistently as

$$S_\theta = \frac{1}{\delta_0} \cdot \frac{|\delta(1.1\theta) - \delta(0.9\theta)|}{0.2} \tag{16}$$

This analysis provides both the numerical threshold required by a tester or controller and the reason for monitoring cylinder-resolved acceleration rather than a single global coefficient: the former retains the imbalance information, whereas the latter is partly masked by the cycle-to-cycle variation. The use of cycle-to-cycle scatter is qualitatively consistent with the experimental combustion variability reported for a common-rail diesel engine [27] and with the cylinder pressure and indicated mean effective pressure variability measured over 200 cycles in a small direct injection diesel engine [36].

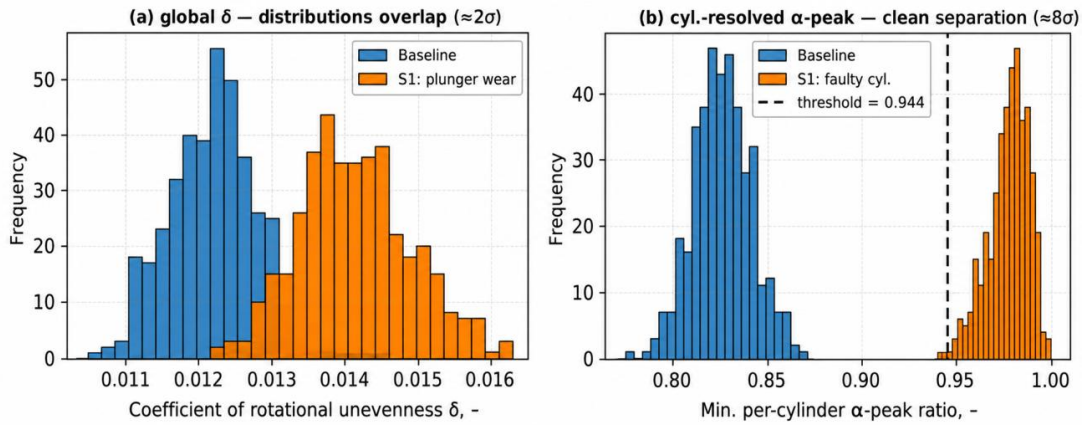


Figure 12. Monte-Carlo separation of healthy and faulty engine by the global coefficient (left) and by the cylinder-resolved peak-acceleration ratio (right)

3.10 Validation Against Published Data and Rated Specifications

Pending a dedicated bench campaign, the model was assessed on three independent aspects. First, its indicated power and torque of 61.0 kW and 291 N·m reproduce the catalogued brake of 59.6 kW and 298 N·m after the application of a realistic mechanical efficiency. The predicted peak cylinder pressure of approximately 6.5 MPa is physically plausible for a naturally aspirated direct-injection diesel of this class. Second, published instantaneous-speed studies show that combustion faults alter phase-resolved crank-speed signatures [4]–[6], [11]–[14], which is in qualitative agreement with Figures 5–7; studies [6] and [13] specifically demonstrate the localisation of the affected cylinder. Transient engine simulations predict the same coupling between the cylinder torque and instantaneous speed [28]. Third, the predicted torsional response was consistent with combustion-related crankshaft vibration studies [37]. The full experimental calibration against the measured cylinder pressure and encoder speed traces remains the next validation step.

3.11 Comparison with Other Diagnostic Approaches

It is useful to place instantaneous speed analysis alongside other established routes for diesel-fault detection. Table 7 compares it with in-cylinder pressure measurement, vibration or acoustic monitoring, and exhaust gas analysis. The speed-based method is low-cost and accessible because it reuses the crankshaft position sensor and flywheel already present in the engine, does not penetrate the combustion chamber, and localises supply imbalance faults well. Its weakness is the limited sensitivity to thermal or atomisation faults that change the combustion shape without substantially changing the delivered mass; Table 4 shows this for coking and low injector pressure, for which pressure or emissions are more direct. Vibration-based reviews have demonstrated the value of non-intrusive condition monitoring [18]. Real-time learning-based classifiers can identify abnormal operating states [20], whereas vibration and acoustic emission studies have shown that fault-sensitive components can be isolated through signal processing [21]. Acoustic studies [23], [38] demonstrate

sensitivity to engine speed, load, and fuel formulation but do not establish cylinder fault localisation. Learning-based classifiers can be highly accurate but require labelled data and do not necessarily return a physical fault parameter. Therefore, the present method is intended as a first-line, cylinder-resolved screen for fuel delivery imbalance, complemented by pressure or emission measurements when a thermal or atomisation defect is suspected.

Table 7. Comparison of crankshaft-speed analysis with other diagnostic approaches

Criterion	Crankshaft speed / accel.	Cylinder pressure	Vibration / acoustic	Exhaust-gas analysis
Sensor cost / intrusiveness	Low; existing CKP sensor	High; in-cylinder transducer	Low–moderate; external	Moderate; gas bench
Cylinder localisation	Good (phase-locked)	Direct, per cylinder	Moderate	Poor (mixed exhaust)
Sensitivity to supply imbalance	High	High	Moderate	Low–moderate
Sensitivity to atomisation / thermal faults	Low	High	Moderate	High
On-board feasibility	High	Low	Moderate	Low

3.12 Diagnostic Recommendations

The calculations support a practical scheme for non-intrusive cylinder-by-cylinder diagnosis built on the angular acceleration $\alpha(\varphi)$ reconstructed from a high-resolution crankshaft position sensor reading the flywheel. The controller or motor tester evaluates the acceleration peak during the power stroke of each cylinder and forms the per-cylinder ratio of Eq. (14), which is below the threshold of Eq. (15) marks the cylinder as weak. Eight fuel system parameters can be addressed in order of their diagnostic weight: (1) hydraulic tightness of the plunger pair, (2) uniformity of the section adjustment, (3) atomisation quality, that is, nozzle coking or wear, (4) injector opening pressure, (5) tightness of the delivery valve, (6) nozzle tightness, (7) condition of the air cleaner, and (8) pressure in the low-pressure line. A localised drop in the acceleration peak of one cylinder, with the overall pattern preserved, indicates a local loss of delivery or poor atomisation in that cylinder, whereas a uniform reduction across all cylinders indicates a general shortage of air or fuel. A simple decision sequence follows. If the acceleration analysis shows a lag in, for example, the fourth cylinder, the cylinder-piston group is first excluded by a relative compression check. The suspect injector is then exchanged with a known-good injector, and if the defect moves with the injector, the nozzle is at fault, whereas if it stays with the cylinder, the corresponding pump section is implicated. Only a standard crankshaft position sensor and a tester are required; therefore, the method can be applied without dismantling the fuel equipment. This is its main practical advantage over bench testing.

4. Conclusions

An integrated model of the MMZ D-243 diesel engine was developed by coupling single-zone cylinder thermodynamics, slider-crank dynamics, and parametric sub-models of fuel and air systems. The numerical independence from the integration step size and tolerances was verified. The main fuel system faults were ranked according to their influence on the coefficient of rotational unevenness. Faults that unbalance cyclic delivery between cylinders dominate: single-section plunger wear increases the coefficient by 19.6%, pump section maladjustment by 13.6%, and delivery valve leakage by 9.3%. Uniform air or fuel restriction slightly decreased the coefficient while reducing the power by as much as 32%. The ranking remained stable when wall heat transfer, operating point, parameter sensitivity, and uncertainty were considered. The Woschni term reduces the absolute power by approximately 11% but changes each fault increment by no more than approximately two percentage points and alters neither its sign nor its rank. The signature of the dominant fault persisted from idle to rated speed and from 30% to full load. The sensitivity study showed that the rotational unevenness is governed far more strongly by the cylinder-to-cylinder delivery balance than by the atomisation quality. Monte Carlo analysis shows that a global coefficient separates healthy and faulty cases by only about two standard deviations, whereas the cylinder-resolved peak acceleration ratio separates them by about eight. Therefore, a threshold of 0.94 for this ratio is proposed for cylinder-by-cylinder screening. The novelty of this study is the direct parametric link between named defects in a mechanically governed fuel system and the instantaneous speed signature, their ranking on a consistent basis, and a statistically grounded threshold for the cylinder-resolved feature. The practical value of this method is that screening requires only a sensor already fitted to the engine. Future work will include bench calibration against measured pressure and encoder speed traces, drivetrain elasticity and torsional vibration in a multi-degree-of-freedom shaft model, a coupled hydraulic model of the high-pressure line and injector, and outputs for brake-specific fuel consumption, nitrogen oxides and smoke.

Acknowledgements

The authors thank the staff of Kazan State Agrarian University for organisational, scientific, and methodological support and the specialists of TPK MTZ-Tatarstan for expert consultation on the operation of BELARUS-series machinery.

Funding
This study was not supported by any grants from funding bodies in the public, private, or not-for-profit sectors.

Declaration of Competing Interests
The authors declare no conflicts of interest.

CRediT Author Contribution Statement
K. Khafizov: Conceptualisation; Methodology; Writing – review & revise
A. Timirzyanov: Methodology; Software; Formal analysis; Visualisation; Supervision; Writing– original draft
R. Khafizov: Validation; Resources; Project administration; Writing – review & revise

Availability of Data and Materials
The numerical datasets and MATLAB scripts used in this study are available from the corresponding author on reasonable request.

Ethics Statement
This study did not involve human participants or animal subjects. Ethical approval was therefore not required.

Generative Artificial Intelligence Disclosure
OpenAI GPT-5.6 Pro was used to assist with language editing, consistency checks, reference formatting, and preparation of the response to editorial comments. The authors retain full responsibility for verifying the technical content, numerical results, interpretations, and final wording before submission.

References
[1] D. K. Dond and N. P. Gulhane, "Effect of injection system parameters on performance and emission characteristics of a small single cylinder diesel engine," *International Journal of Automotive and Mechanical Engineering*, vol. 18, no. 2, pp. 8790–8801, 2021. https://doi.org/10.15282/ijame.18.2.2021.17.0673.
[2] T. Osipowicz and R. Grzejda, "Influence of wear on precision pair components in modern fuel injectors on the operating and environmental performance of a compression-ignition engine," *International Journal of Automotive and Mechanical Engineering*, vol. 22, no. 3, pp. 12614–12626, 2025. https://doi.org/10.15282/ijame.22.3.2025.6.0963.
[3] M. Karczewski and K. Koliński, "Diagnostics of common rail components based on pressure curves in the fuel rail," *Combustion Engines*, vol. 173, no. 2, pp. 3–8, 2018. https://doi.org/10.19206/CE-2018-201.
[4] J. Yang, L. Pu, Z. Wang, Y. Zhou, and X. Yan, "Fault detection in a diesel engine by analysing the instantaneous angular speed," *Mechanical Systems and Signal Processing*, vol. 15, no. 3, pp. 549–564, 2001. https://doi.org/10.1006/mssp.2000.1344.
[5] T. R. Lin, A. C. C. Tan, L. Ma, and J. Mathew, "Condition monitoring and fault diagnosis of diesel engines using instantaneous angular speed analysis," *Proceedings of the Institution of Mechanical Engineers, Part C: Journal of Mechanical Engineering Science*, vol. 229, no. 2, pp. 304–315, 2015. https://doi.org/10.1177/0954406214533253.
[6] D. Kazienko and L. Chybowski, "Instantaneous rotational speed algorithm for locating malfunctions in marine diesel engines," *Energies*, vol. 13, no. 6, Art. no. 1396, 2020. https://doi.org/10.3390/en13061396.
[7] J. Jiang, H. Li, Z. Mao, *et al.*, "A digital twin auxiliary approach based on adaptive sparse attention network for diesel engine fault diagnosis," *Scientific Reports*, vol. 12, Art. no. 675, 2022. https://doi.org/10.1038/s41598-021-04545-5.
[8] S. Li, Z. Liu, Y. Yan, R. Wang, E. Dong, and Z. Cheng, "Research on diesel engine fault status identification method based on synchrosqueezing S-transform and vision transformer," *Sensors*, vol. 23, no. 14, Art. no. 6447, 2023. https://doi.org/10.3390/s23146447.
[9] X. Wang, P. Zhang, W. Gao, Y. Li, Y. Wang, and H. Pang, "Misfire detection using crank speed and long short-term memory recurrent neural network," *Energies*, vol. 15, no. 1, Art. no. 300, 2022. https://doi.org/10.3390/en15010300.
[10] S. Xu, J. Lei, C. Qin, Z. Zhang, J. Tao, and C. Liu, "A domain-adversarial wide-kernel convolutional neural network for noisy domain adaptive diesel engine misfire diagnosis," *IEEE Transactions on Instrumentation and Measurement*, vol. 73, Art. no. 3506819, 2024. https://doi.org/10.1109/TIM.2023.3343796.
[11] R. Hasegawa and Y. Aoyama, "A study on misfire detection by calculating crank angular velocity considering in-cylinder gas properties," *International Journal of Engine Research*, vol. 25, no. 10, pp. 1868–1878, 2024. https://doi.org/10.1177/14680874241261419.
[12] J. Gan, H. Jin, Q. Shang, and C. Sheng, "A new method of intelligent fault diagnosis of ship dual-fuel engine based on instantaneous rotational speed," *Journal of Marine Science and Engineering*, vol. 12, no. 11, Art. no. 2046, 2024. https://doi.org/10.3390/jmse12112046.
[13] Z.-L. Tang, J.-Z. Li, C.-X. Jiang, *et al.*, "Identifying fault cylinder location of diesel engines based on instantaneous speed," *Mechanical Systems and Signal Processing*, vol. 225, Art. no. 112301, 2025. https://doi.org/10.1016/j.ymssp.2025.112301.
[14] Y. Huang, Z. Li, J. Wang, C. Liu, and B. Hu, "Fire fault diagnosis based on signal EEMD of diesel engine crankshaft instantaneous speed," *Transactions of the Beijing Institute of Technology*, vol. 45, no. 4, pp. 384–390, 2025. https://doi.org/10.15918/j.tbit1001-0645.2024.165.
[15] V. N. Guerra, B. M. Castro, D. H. C. S. S. Martins, R. H. R. Gutiérrez, and U. A. B. V. Monteiro, "Framework for single misfire identification in a marine diesel engine using machine learning," *Journal of Marine Science and Application*, vol. 24, no. 5, pp. 1086–1102, 2025. https://doi.org/10.1007/s11804-025-00752-y.

[16] C. Patil, G. Theotokatos, and K. Tsitsilonis, "Data-driven model for marine engine fault diagnosis using in-cylinder pressure signals," *Journal of Marine Engineering & Technology*, vol. 24, no. 1, pp. 70–82, 2025. https://doi.org/10.1080/20464177.2024.2432777.

[17] J. Radić, M. Šarić, and A. Rubić, "Spectral-based fault detection method in marine diesel engine operation," *Sensors*, vol. 25, no. 18, Art. no. 5669, 2025. https://doi.org/10.3390/s25185669.

[18] O. Afanaseva, D. Pervukhin, and A. Khatrusov, "Vibration-based condition monitoring of diesel engines in industrial energy applications: A scoping review," *Energies*, vol. 18, no. 21, Art. no. 5717, 2025. https://doi.org/10.3390/en18215717.

[19] A. Helali, I. Belkacem, J. Abdellaoui, and A. Zegnani, "Vibration analysis for diagnosis of diesel engines with air flow sensor failure," *Technologies*, vol. 13, no. 9, Art. no. 380, 2025. https://doi.org/10.3390/technologies13090380.

[20] S. M. Shahid, S. Ko, and S. Kwon, "Real-time abnormality detection and classification in diesel engine operations with convolutional neural network," *Expert Systems with Applications*, vol. 192, Art. no. 116233, 2022. https://doi.org/10.1016/j.eswa.2021.116233.

[21] S. Allam, M. Abdo, and M. Rabie, "Diesel engine fault detection using vibration and acoustic emission signals," *International Journal of Advances in Scientific Research and Engineering*, vol. 4, no. 12, pp. 86–93, 2018. https://doi.org/10.31695/IJASRE.2018.33005.

[22] K. Indriawati, G. F. Yugoputra, N. N. Habibah, and R. Yudhanto, "Artificial neural network-based fault detection system with residual analysis approach on centrifugal pump: A case study," *International Journal of Automotive and Mechanical Engineering*, vol. 20, no. 1, pp. 10285–10297, 2023. https://doi.org/10.15282/ijame.20.1.2023.10.0795.

[23] J. M. Zikri, M. S. M. Sani, and F. Jaliliantabar, "Optimization of noise emission level in diesel engine with biodiesel application using response surface methodology," *International Journal of Automotive and Mechanical Engineering*, vol. 21, no. 4, pp. 11909–11924, 2024. https://doi.org/10.15282/ijame.21.4.2024.13.0916.

[24] M. Asad, U. Iftikhar, D. Abbasi, and M. B. Jamil, "A comparative analysis of regression modelling and artificial neural networks for diesel engine performance prediction," *International Journal of Automotive and Mechanical Engineering*, vol. 23, no. 1, pp. 13339–13355, 2026. https://doi.org/10.15282/ijame.23.1.2026.13.1011.

[25] B. Lakshminarayana, A. Kulkarni, G. H. Narayanappa, *et al.*, "Supervised learning technique to develop predictive regression model and performance evaluation of dual bio-diesel blends," *Results in Chemistry*, vol. 26, Art. no. 103330, 2026. https://doi.org/10.1016/j.rechem.2026.103330.

[26] M. J. Noroozi and M. Seddiq, "Effects of post-injection characteristics on the combustion, emission, and performance in a diesel-syngas reactivity controlled compression ignition engine," *International Journal of Automotive and Mechanical Engineering*, vol. 18, no. 3, pp. 9006–9021, 2021. https://doi.org/10.15282/ijame.18.3.2021.13.0690.

[27] A. Şanlı and İ. T. Yılmaz, "Cycle-to-cycle combustion analysis in hydrogen fumigated common-rail diesel engine," *Fuel*, vol. 320, Art. no. 123887, 2022. https://doi.org/10.1016/j.fuel.2022.123887.

[28] Z. S. Filipi and D. N. Assanis, "A nonlinear, transient, single-cylinder diesel engine simulation for predictions of instantaneous engine speed and torque," *Journal of Engineering for Gas Turbines and Power*, vol. 123, no. 4, pp. 951–959, 2001. https://doi.org/10.1115/1.1365122.

[29] I. V. Leonov and D. I. Leonov, *Theory of Machines and Mechanisms: Fundamentals of Design Based on Dynamic Criteria and Economic Indicators*. Moscow, Russia: Vysshee Obrazovanie, 2008 (in Russian).

[30] J. B. Heywood, *Internal Combustion Engine Fundamentals*, 2nd ed. New York, NY, USA: McGraw-Hill Education, 2018.

[31] V. N. Lukanin, K. A. Morozov, A. S. Khachiyan, *et al.*, *Internal Combustion Engines, Vol. 1: Theory of Working Processes*, V. N. Lukanin, Ed., 2nd ed. Moscow, Russia: Vysshaya Shkola, 2005 (in Russian).

[32] I. I. Vibe, *New Information on the Working Cycle of Engines: Combustion Rate and the Engine Cycle*. Moscow–Sverdlovsk, USSR: Mashgiz, 1962 (in Russian).

[33] G. Woschni, "A universally applicable equation for the instantaneous heat transfer coefficient in the internal combustion engine," SAE Technical Paper 670931, 1967. https://doi.org/10.4271/670931.

[34] Q. Lan, L. Fan, Y. Bai, Y. Gu, and L. Wen, "Experimental and numerical investigation on pressure characteristics of the dual-valve controlled fuel system for low-speed diesel engines," *Fuel*, vol. 294, Art. no. 120501, 2021. https://doi.org/10.1016/j.fuel.2021.120501.

[35] D. W. Green and M. Z. Southard, Eds., *Perry's Chemical Engineers' Handbook*, 9th ed. New York, NY, USA: McGraw-Hill Education, 2018.

[36] M. H. Ali, A. Abdullah, M. H. Mat Yasin, and M. K. Kamarulzaman, "Cyclic pressure variations in a small diesel engine fueled with biodiesel and antioxidant blends," *International Journal of Automotive and Mechanical Engineering*, vol. 17, no. 2, pp. 7851–7857, 2020. https://doi.org/10.15282/ijame.17.2.2020.04.0585.

[37] P. Charles, J. K. Sinha, F. Gu, L. Lidstone, and A. D. Ball, "Detecting the crankshaft torsional vibration of diesel engines for combustion related diagnosis," *Journal of Sound and Vibration*, vol. 321, no. 3–5, pp. 1171–1185, 2009. https://doi.org/10.1016/j.jsv.2008.10.024.

[38] M. S. Mohd Sani, J. M. Zikri, and A. Abdul Adam, "Sound intensity mapping on single cylinder direct injection diesel engine with the application of palm oil methyl ester biodiesel," *International Journal of Automotive and Mechanical Engineering*, vol. 18, no. 2, pp. 8833–8844, 2021. https://doi.org/10.15282/ijame.18.2.2021.21.0677.